Ocean Engineering, Volume 240, November 2021, Article number 109967
DOI:10.1016/j.oceaneng.2021.109967

Numerical modelling of new flap-gate type breakwater in regular and solitary waves using one-fluid formulation

Songgui Chen[a], Jingru Xing[b], Liang Yang[b,*], Huaqing Zhang[a,**], Yingni Luan[a], Hanbao Chen[a], Haiyuan Liu[a]

[a] *Tianjin Research Institute for Water Transport Engineering, China*
[b] *Department of Energy and Power, Cranfield University, UK*

Abstract

Breakwater is commonly used infrastructure for protecting coastal zones from waves and tsunamis. Computational modelling is frequently employed for prediction and validation of the breakwater design. Potential flow based models may not be ideal for such applications due to large energy dissipation. We apply the Computational Fluid Dynamics (CFD) to study the waves and breakwater interaction problem. In this work, we benchmark the performance of a new type of flap-gate breakwater in regular waves (airy wave theory and second order Stokes wave theory), where the multiphase Navier-Stokes equations are solved and the structure of breakwater is considered as one phase of fluid within the 'one-fluid' framework. In this way, the computational costs will be reduced as the same level as the numerical wave tank alone. We conduct a grid refinement study and compare results to experiments to investigate accuracy. The result shows a good agreement with the experimental data. Further, we use the validated model for sensitivity studies for different settings of flap-gate, and the solitary waves paradigm for tsunamis. The proposed novel numerical tool allows us to study large parametric spaces, impact of breaking waves, load and pressure producing process and interaction time.

Keywords: Computational Fluid Dynamics (CFD) flap-gate breakwater one-fluid formulation wave-structure interaction

*Corresponding author: L. Yang, liang.yang@cranfield.ac.uk
**Corresponding author: H. Zhang: tjzhq1@163.com

Preprint submitted to Ocean Engineering

- Performance of flap-gate breakwater in different settings is evaluated by using CFD
- The flap-gate breakwater is modelled as a phase of fluid within the 'one-fluid' framework, the dynamics of fluid-structure interaction is solved within the fluid solver
- Good comparison with experimental result for regular waves, including airy wave theory and 2nd Stokes wave.
- Solitary wave impact with breakwater is studied for analogy of tsunamis

1. Introduction

With the development of shipment, numerous coastal areas are gradually becoming major economic centres of the country [1, 2]. They have a rapidly growing population and a progressively stronger industry [3, 4]. However, these areas are also more vulnerable to coastal environmental problems and even to disasters such as tsunamis or floods, especially in developing countries [5, 6, 7]. Therefore, a series of breakwaters are often placed in ports, jetty and human settlement as a local protection response. They are always liable for wave attenuation, wave dispersion and shoreline control [8, 9].

Currently there are mainly two types of breakwater structures, namely fixed breakwaters and floating breakwaters [10, 11]. The fixed type includes the block-work breakwater, caisson and piled breakwater [10]. Floating breakwaters can be divided into seven main categories, box type, pontoon type, frame type, mat type, tethered float type, horizontal plate type and other types [11]. By the mechanisms of breakwater structures, they can also be classified into three types of reflecting type, disturbing type, and friction type [11, 12, 13]. Fixed breakwaters belong to the reflective category. Their concrete walls require to be sufficiently firm to sustain the impact loads from the wave smashing [14, 15]. Also in the reflective category are the floating box-type and pontoon-type breakwaters [11].

In this work, we are interested in a new type of breakwater, the flap-gate type. The flap-gate breakwater, which combines the advantages of fixed and floating types, is also classified as reflecting type. There are two examples of such breakwater, depending on whether the gate is rotated counterclockwise or clockwise facing the wave. One practical application is the 'MOSE' (MOdulo Sperimentale Elettromeccanico) system. These flap-gate barriers (MOSE) are the defence system which, in due course, separates the Venetian Lagoon from the Adriatic Sea, protecting the city of Venice from high tides and storm surges [16, 17]. When in operation, compressed air is pumped in and replaces the water inside the gates. The gates rotate clockwise around the hinge axis and

rise until they emerge from the water surface to prevent the high tide. When the tide returns to normal, the gates are filled with water and they lie on the floor of the lagoon inlets [18]. Another typical flap-gate example is a flap-gate type movable seawall. It is also known as 'neo RiSe' (No Energy, No Operation, Rising Seawall) [19, 20, 21]. The wall-flap-gate is an improved version of 'neo RiSe'. Kimura [19] conducted hydrodynamic experiment and various prototype tests on the wall-flap-gate. The structure is positioned at a certain distance from the ground. It blocks the tsunami or flood flow by rotating counterclockwise and closing the ventilator with the gate. The structure has proven to be strong and efficient enough to be used to protect coastal buildings from inundation by tsunamis or floods. The Hamaoka Nuclear Power Station has practical wall flap doors installed on its outer walls [19].

The flap-gate breakwater in this study tends to be similar to the 'neo RiSe'. It works automatically by its own buoyancy without the support of external pumps. As the incoming the inundation water surges towards it, it rotates and the movement appears to flap. For water close to the shore it then acts as a wave maker. In other words, breakwater converts violent waves of high frequency and wave height into waves of lower frequency and wave height with less impact. It attenuates waves by reflection from the plate and dissipates wave energy by wave slamming phenomena. It is aiming to minimise damage from high-energy waves by the forces of nature itself [19].

Numerical simulation of the dissipated wave energy is challenging for flap-gate type of breakwater. The traditional method to tackle this is to separate it into two problems, hydrodynamics and rigid body dynamics, either in time or frequency domain. A potential flow theory is often used [22, 23, 24, 25], but the simplification of potential flow models limits the application. With a significant advancement in computational fluid dynamics (CFD) and computing power, the use of CFD model is a viable approach. Although CFD is considered as computational expensive, they can provide an accurate and high fidelity modelling for different problems.

The interface capturing, e.g. level set methods [26, 27] or volume of fluid

methods [28] or interface tracking methods with two-phase immiscible flow model is commonly used for the CFD based wave modelling approaches. It is noticed that the miscible flow model, e.g. the interpenetrating model, could also be used for wave and structure interaction modelling [29].

In the present numerical study, we presented alternative approaches for solving wave-structure interaction problems using one-fluid formulation and investigated the effectiveness of the new type of flap-gate breakwater. We will verify and validate the multiphase solver in terms of wave generation and propagation. Then, the verified and validated model is applied for the flap-gate and wave interaction and compared with the experiment. In the last, we investigate the breakwater under tsunamis like solitary waves. This enables us to investigate a large variety of wave height. All the simulations are conducted in two-dimensional domain.

The outline of the paper is organised as follows. Section 2 introduces the 'one-fluid' numerical models for multiphase flow interaction with rigid structure, as well as the numerical algorithm. Section 3 provides a detailed description of the experimental layout and testing conditions. Section 4 discusses the details of numerical results compared with the experiment. Section 5 presents the efficiency of breakwater under solitary waves. Finally, conclusions are drawn in Section 6.

2. Numerical model

2.1. Multiphase flow

The unsteady incompressible viscous flow, occupying the domain Ω_f, which can be described in the spatial coordinates as,

$$\rho\left[\frac{\partial \boldsymbol{u}}{\partial t}+(\boldsymbol{\nabla u})\boldsymbol{u}\right]=-\boldsymbol{\nabla}p+\boldsymbol{\nabla}\cdot 2\mu\mathbf{D}(\boldsymbol{u})+\rho\boldsymbol{g} \qquad \text{in } \Omega_f \qquad (1a)$$

$$\boldsymbol{\nabla}\cdot\boldsymbol{u}=0 \qquad \text{in } \Omega_f \qquad (1b)$$

which represents the strong form of the incompressible Navier-Stokes equations, where $\mathbf{D}(\boldsymbol{u})=\frac{1}{2}(\boldsymbol{\nabla u}+(\boldsymbol{\nabla u})^T)$ is the strain rate tensor, ρ is the density field

of the fluid and μ is the dynamic viscosity, $\boldsymbol{g}$ the gravitational acceleration respectively. With suitable initial/boundary condition, the system is closed. In this paper, the fluid and water is assumed to be the incompressible viscous flow by Eq. (1). The density and viscosity of the system is determined by the combination of smoothed Heaviside function

$$\rho = \rho_a H_a + \rho_w H_w; \quad \mu = \mu_a H_a + \mu_w H_w \tag{2}$$

where $\Omega_f = \Omega_a \cup \Omega_w$ (in the absence of surface tension), where the subscript a, w denotes the air and water.

2.2. Interface capturing method

The numerical wave tank solves the Navier-Stokes equations to describe in detail the incompressible flow of two immersible fluid (water and air). The location of the free surface is represented by zero level set of a signed distance function $\phi(\boldsymbol{x}, t)$. The evolution equation of an interface moving in a medium with velocity $\boldsymbol{u}$, is defined in an non-conservative form as

$$\frac{\partial \phi}{\partial t} + \boldsymbol{u} \cdot \boldsymbol{\nabla} \phi = 0 \tag{3}$$

The above Level Set equations can be convected using standard numerical method for a hyperbolic equations. The Eikonal equation $|\boldsymbol{\nabla u}| = 1$ is valid. Reinitialisation is required to maintain a signed distance function.

2.3. Numerical wave tank: wave generation and absorption

The wave generation is acquired by wave generation zone and wave absorption zone. The free surface and inlet velocity is described at the inlet boundary condition. The values are obtained from airy wave theory. At the end of the wave flume, the waves should be dissipated to avoid the reflections by using a relaxation method. In the case of first order linear waves, the horizontal and vertical velocity u and v and the wave height for the free surface location are

given as:

$$
\begin{aligned}
u(x,z,t) &= \frac{\pi H}{T}\frac{\cosh[k(z+d)]}{\sinh kd}\cos\theta \\
v(x,z,t) &= \frac{\pi H}{T}\frac{\sinh[k(z+d)]}{\sinh kd}\sin\theta \\
\phi(x,z,t) &= \frac{H}{2}\cos\theta - z + d
\end{aligned}
\tag{4}
$$

The wave number is defined as $k = \frac{2\pi}{L}$ and the wave phase $\theta = kx - \omega t$, where H is the wave height, L is wavelength, T is the wave period, ω the angular wave frequency, and z is the vertical coordinate. Stokes wave theory was implemented with second order component. The velocity and level set function becomes [30, 31]:

$$
\begin{aligned}
u(x,z,t) &= \frac{\pi H}{T}\frac{\cosh[k(z+d)]}{\sinh kd}\cos\theta + \frac{3H^2\pi k}{8T}\frac{\cosh[2k(z+d)]}{\sinh^4 kd}\cos 2\theta \\
v(x,z,t) &= \frac{\pi H}{T}\frac{\sinh[k(z+d)]}{\sinh kd}\sin\theta + \frac{3H^2\pi k}{8T}\frac{\sinh[2k(z+d)]}{\sinh^4 kd}\sin 2\theta \\
\phi(x,z,t) &= \frac{H}{2}\cos\theta + \frac{\pi H^2}{8L}\frac{\cosh kd}{\sinh^3 kd}(2+\cosh 2kd)\cos 2\theta - z + d
\end{aligned}
\tag{5}
$$

The wave steepness H/L and relative depth h/L illustrate the behaviour of the wave.

The absorption zone is added to dissipate the velocity and force the free surface to the still water level using a relaxation method [32], with a relaxation length equal two wavelengths. Use Eq.6 to generate the absorption zones

$$
p(\tilde{x}) = 1 - \frac{e^{(\tilde{x}^{3.5})} - 1}{e - 1} \quad \text{for} \quad \widetilde{x} \in [0,1] \tag{6a}
$$

$$
u' = p(\tilde{x})u \tag{6b}
$$

$$
v' = p(\tilde{x})v \tag{6c}
$$

where $\tilde{x}$ is scaled to the length of the relaxation zone. $k\tilde{x}$ is subtractive scale factor equation. u and v are the velocity components of the velocity field in the horizontal (x) and vertical (y) directions, respectively. Reynolds-averaged Navier-Stokes (RANS) zero-equation turbulence model are used in the simulation [33].

2.4. Dynamics of flap gate

Flap gate breakwater within the domain taken into account using the 'one-fluid' formulation [34]. In contrast with a wave energy converter [35], there is no damping or stiffness added to the flap gate system. Subject to the kinematic constraint, the dynamics of the flap plate can be written in a new form, comparable with Navier-Stokes Eqs. (1)

$$\rho\left[\frac{\partial \boldsymbol{u}}{\partial t}+(\boldsymbol{\nabla u})\boldsymbol{u}\right]=-\boldsymbol{\nabla}p+\boldsymbol{\nabla}\cdot\mathbf{D}[\boldsymbol{\lambda}]+\rho\boldsymbol{g} \tag{7a}$$

$$\boldsymbol{u}=\boldsymbol{\omega}\times(\boldsymbol{x}-\boldsymbol{x}_0) \tag{7b}$$

Above Eq. (7) is the strong form of the governing equation for the dynamics of flap plate. Compared with the N-S Eq. (1), the only difference is the evaluation of $\boldsymbol{\nabla}\cdot\mathbf{D}[\boldsymbol{\lambda}]$. The rigidity force is clearly stated on the continuum level.

2.5. Overall fluid-structure interaction

In the case of immersed methodologies, the explicit use of the jump conditions is avoided by means of a 'smooth regularisation' of the interface. With the new formulation Eq. (7) for the rigid body dynamics, the conservation equation for the linear momentum for three-phase system can be expressed in a single equation in the whole domain $\Omega=\Omega_a\cup\Omega_w\cup\Omega_r$ (in the absence of surface tension), where the subscript a,w,r denotes the air, water and rigid body phases, respectively.

$$\begin{aligned}
\rho\left[\frac{\partial \boldsymbol{u}}{\partial t}+(\boldsymbol{\nabla u})\boldsymbol{u}\right]&=-\boldsymbol{\nabla}p+\boldsymbol{f}+\rho\boldsymbol{g} \quad && \text{in } \Omega=\Omega_a\cup\Omega_w\cup\Omega_r\\
\boldsymbol{\nabla}\cdot\boldsymbol{u}&=0 && \text{in } \Omega\\
\boldsymbol{u}&=\boldsymbol{\omega}\times(\boldsymbol{x}-\boldsymbol{x}_0) && \text{in } \Omega_r
\end{aligned}\quad . \tag{8}$$

where $\rho=\rho_r H_r+\rho_w H_w+\rho_a H_a$. In these expressions, H_a is the generalised Heaviside function for a phase a, which is defined as

$$H_a(\boldsymbol{x})=\begin{cases}1 & \text{if} \quad \boldsymbol{x}\in\Omega_a\\ 0 & \text{if} \quad \boldsymbol{x}\notin\Omega_a\end{cases}\quad . \tag{9}$$

In the Eq. (8), the force $\boldsymbol{f}$ is defined on each phase

$$\boldsymbol{f} = \begin{cases} \boldsymbol{\nabla} \cdot 2\mu_a \mathbf{D}(\boldsymbol{u}) & \text{air} \\ \boldsymbol{\nabla} \cdot 2\mu_w \mathbf{D}(\boldsymbol{u}) & \text{water} \\ \boldsymbol{\nabla} \cdot \mathbf{D}[\boldsymbol{\lambda}] & \text{rigid} \end{cases} . \tag{10}$$

The formulation is named 'one-fluid' because the governing Eq. (8) is similar to those of the single phase N-S Eq. (1). The above Eq. (8) is a rewrite of the three-phases equations for the whole domain and satisfies the non-slip boundary on the interface without resorting to the jump condition.

2.6. Numerical and discretisation scheme

From the spatial discretisation point of view, we employ a Cartesian staggered Finite Volume scheme (Marker-and-Cell grid) and a level set methodology to describe the evolution of the various interacting phases. The convective terms of N-S equations are discretised with a second order TVD Runge-Kutta scheme in the conservative framework. For the time treatment of the momentum and the level set equations, a second order accurate Runge-Kutta scheme is employed. Adaptive time stepping is used to control the Courant-Friedrichs-Lewy (CFL) number.

2.7. Numerical result for periodic waves

We first validate the periodic waves for a wave propagation in 2D. Six cases are tested including linear waves and 2nd order Stokes, where the wave condition table is given in Tab. 1. The wave height $H = 0.1$ m and a wave length $L = 2$ m for a still water depth of $d = 0.5$ m in a 20 m long wave flume is in the region Stokes theory, but we followed the work [32] using linear wave theory for the wave generation and validation. The CFL number is kept as 0.5. Fig. 1 shows the sketch of the horizontal velocity component. Fig. 2 shows the grid convergence from $dx = 0.08$ to $dx = 0.01$ m under four series of meshes. On the coarse mesh $dx = 0.08$, it shows a large in phase error and amplitude dissipation. The results show a good agreement with the analytical values.

Cases	Wave Steepness	Mesh resolution (m)	Simulation boundary
1	0.05	0.08	linear theory
2	0.05	0.04	linear theory
3	0.05	0.02	linear theory
4	0.05	0.01	linear theory
5	0.08	0.02	linear theory
6	0.08	0.02	2nd Stokes theory

Table 1: Numerical validation cases for periodic waves.

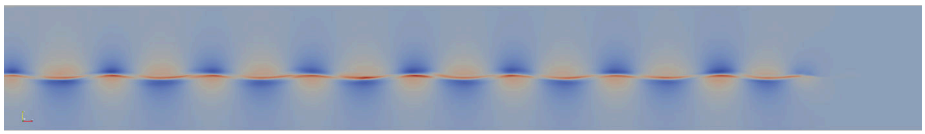

Figure 1: Sketch of the numerical wave tank. The contour shows the horizontal velocity component under meshsize $dx = 0.02$ m.

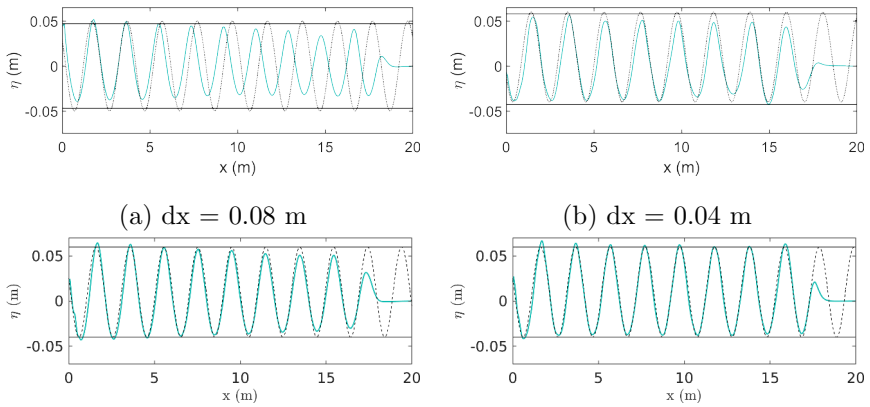

(a) dx = 0.08 m (b) dx = 0.04 m

(c) dx = 0.02 m (d) dx = 0.01 m

Figure 2: Grid convergence test in a 20 metre 2D wave tank with wave height $H = 0.1$ m, wave length $L = 2$ m. The black dash line shows the wave theory.

The wave height $H = 0.16$ m with a wave steepness 0.08, was tested using airy wave theory and 2nd order Stokes theory under mesh resolution $dx = 0.02$, measured at location 5 m, which is shown in Fig. 3. It can be observed that

crests in 2nd order Stokes are steeper than for airy waves.

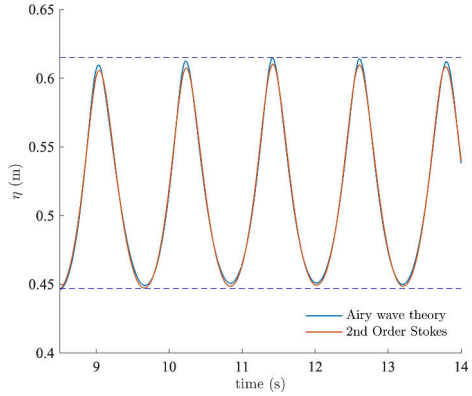

Figure 3: Comparison of surface elevation between airy wave theory and 2nd order Stokes wave theory for generation periodic waves for wave steepness 0.08.

3. Experimental layout and testing conditions

The experiment was conducted in a wave flume in Tianjin Research Institute for Water Transport Engineering, Tianjin, China. The wave flume is 68 m long, 1 m deep and 1 m wide, and waves were generated with a piston type wave maker equipped with an active wave absorption system, as shown in Fig. 4. Based on the dimensions of the experimental wave flume, the geometric scale of the experimental model was designed to be 1:30. The water depth of the flume is 0.50 m, which corresponds to a real water depth of 15 m. The numerical wave tank reproduces the experimental flume arrangement and the schematic diagrams of the two are shown in Fig. 5 and Fig. 6.

The flap-gate breakwater is arranged in the middle of the flume, hinged to the seabed at its ground end. Experiments were carried out with various lengths of breakwaters and their initial downward angle, but ensuring that the initial vertical projection height of all the breakwaters was 0.7 m. Each breakwater consists of two materials, PVC grey plastic sheet (1750 kg/m ^{3}) and EPE foamed plastics (17 kg/m ^{3}), 0.12 m and 0.3 m thick respectively, i.e. an overall average

Figure 4: Wave flume at TIWTE.

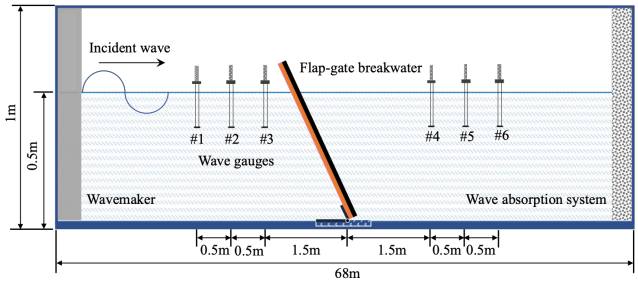

Figure 5: Schematic diagrams of the physical experiment. 6 gauges are registering the wave amplitude at g1-9.

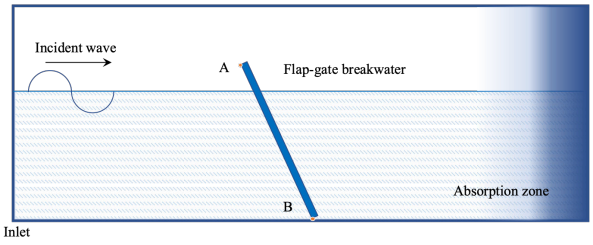

Figure 6: Schematic diagrams of the numerical wave tank, for simplicity, the breakwater is considered as a uniform density.

density of 510kg/m ^{3} with a thickness of 0.42 m. There are no constraints on the flap's rotation motion.

The physical positions of the 6 wave gauges are at a distance of 1.5m from the front and rear of the breakwater, with 0.5 m intervals. They are used to record
175 the surface elevation with a sampling frequency of 100Hz. For clarity, the part of the physical flume reproduced in the numerical domain is also highlighted.

The vertical distance of each transducer from the toe of the wall is given in Table 2.

Wave gauges location	g1	g2	g3	g4	g5	g6
Distance from the breakwater (m)	-2.5	-2.0	-1.5	1.5	2.0	2.5

Table 2: Vertical distance of the surface transducers from breakwater, g1 to g6.

4. Numerical comparison for regular waves

In order to verify the numerical method and validation of the mathematical model, we will first reproduce the physical experiments in Section 3. A computational domain 15 m long and 1.0 m high was used in the numerical simulations. The inflow boundary condition was used with a relaxation zone to avoid reflection. Three sets of grid resolutions with $\Delta x = 0.02$ m, $\Delta x = 0.01$ m, $\Delta x = 0.005$ m were used to check the accuracy and convergence.

We evaluate three types of designs for plate angle 30, 45 and 60 degrees, with a length of 140, 99 and 80.2 respectively. The experiment was conducted with water depth $d = 0.5$ m and details of the settings are shown in Fig. 5. Fig. 7 compared the time history of wave surface elevation between numerical results and experimental data at $H = 0.16$ m, $L = 2.0$ m for angle 30 and $L = 1.4$ m using 2nd order Stokes wave theory. The time series of regular wave interaction with flap-gate breakwater: time evolution of the free surface, breakwater and vorticity contours of the fluids, vorticity contours ($-50 \leq \omega \leq 50$) is shown in Fig. 8.

	mesh size (m)	numbers of cells
1	$\Delta x = 2 \times 10^{-2}$	750×50
2	$\Delta x = 1 \times 10^{-2}$	1500×100
3	$\Delta x = 5 \times 10^{-3}$	3000×200

Table 3: Grid resolution for numerical comparison for regular waves.

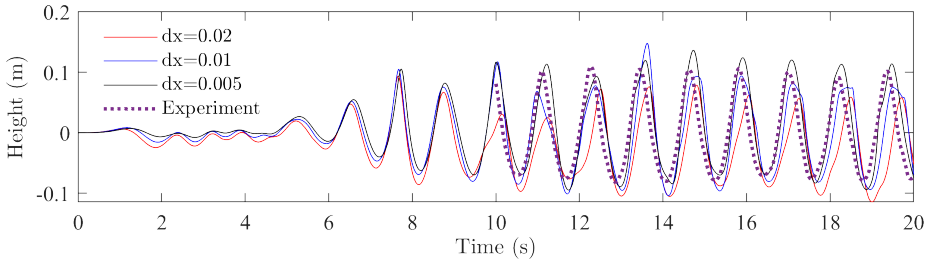

(a) Surface elevation at water gauge 1, before the breakwater.

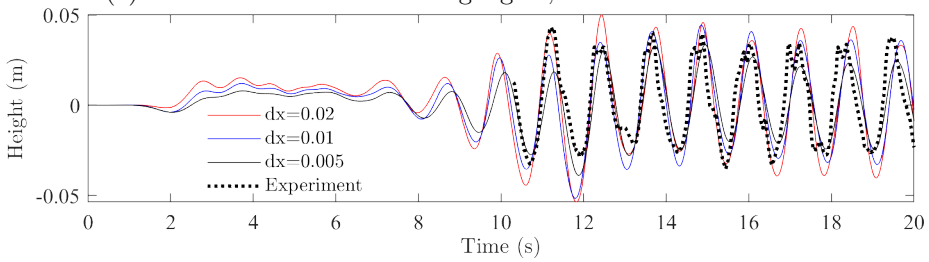

(b) Surface elevation at water gauge 4, after the breakwater.

Figure 7: Time history of wave surface elevation between numerical results and experimental data at $H = 0.16$ m, $L = 2.0$ m for angle 30 and $L = 140$mm from $t = 0$ s to $t = 20$ s.

The transmission coefficients are defined as ratio of the downstream wave height to upstream wave height, shown in the Table 4. Both experimental and numerical shows that 30 degree plate gate breakwater is efficient and has a significant small transmission coefficient. In the case of 60 degree, the breakwater acts as a wave maker and transfers most of its energy. As a result, the system may be efficient with an increasing water depth, e.g. induced by storm surge.

Angle (deg)	Length (cm)	Exp. transmission coef.	Simulation transmission coef.
30	140.0	0.42	0.45
45	99.0	0.83	0.80
60	80.2	0.92	0.89

Table 4: Designed physical parameters for different angles for wavelength $L = 2$m and wave height $H = 0.16$ m.

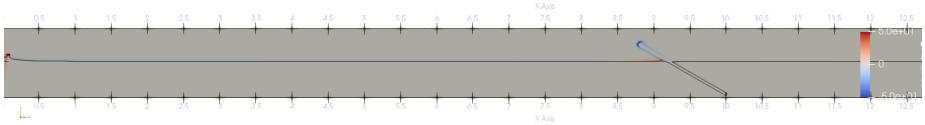

(a) t = 0.0 s

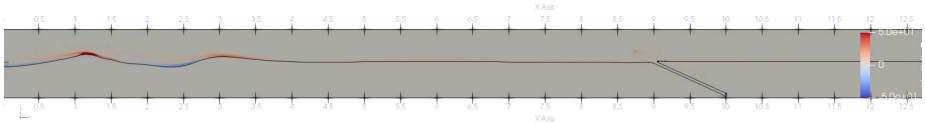

(b) t = 3.0 s

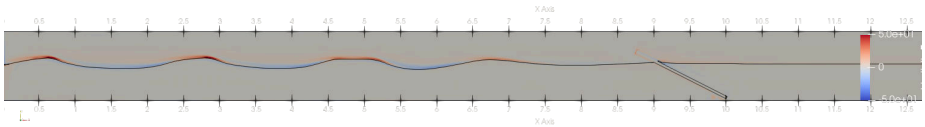

(c) t = 6.2 s

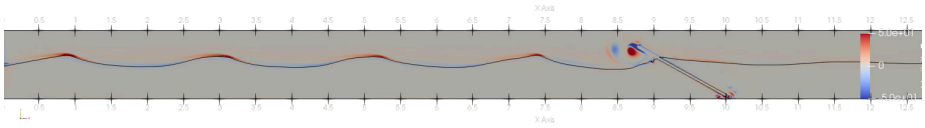

(d) t = 10.0 s

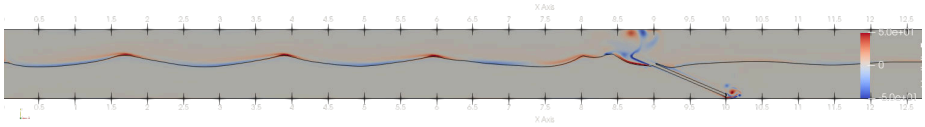

(e) t = 11.5 s

Figure 8: Time series of regular wave interaction with flap-gate breakwater: time evolution of the free surface, breakwater and vorticity contours of the fluids, vorticity contours ($-50 \leq \omega \leq 50$). Water density $\rho_w = 1.0$ g/cm^3, air density $\rho_a = 1.0 \times 10^{-3}$ g/cm^3, breakwater density $\rho_s = 0.5$ g/cm^3, mesh size 3000×200.

5. Tsunami-like solitary waves

In this section, we will evaluate the performance of the new flap-gate breakwater under extreme waves, e.g. tsunamis. Solitary waves have been used extensively to model tsunamis in experimental and analytical studies [36]. Using the validated numerical models, simulations of interactions between solitary waves and the breakwater are performed. The simulation domain is chosen as

8 m long to save computational time. Inlet boundary condition follows the analytical solution of a solitary wave [37].

The solitary wave height is from 0.05 m to 0.25 m and the water depth is 0.5 m in the wave flume. The cases with highest wave height $h = 0.25$ m are displayed by using a fluid mesh refinement study, with meshes of 375×70, 750×140 and 1500×280. The gauge location is the same as in the previous case. Two pressure monitoring points are added at the left corner in the numerical wave tank, shown in Fig. 6. The reflection coefficients are defined as the

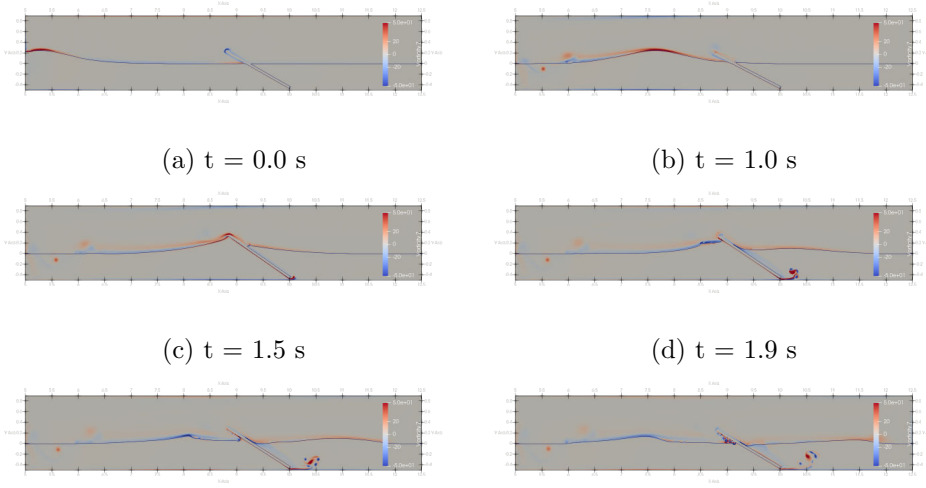

(a) t = 0.0 s (b) t = 1.0 s

(c) t = 1.5 s (d) t = 1.9 s

(e) t = 2.2 s (f) t =2.5 s

Figure 9: Snapshot of solitary wave interaction with flap-gate breakwater: time evolution of the free surface, breakwater and vorticity contours of the fluids, vorticity contours ($-50 \leq \omega \leq 50$). Water density $\rho_w = 1.0$ g/cm^3, air density $\rho_a = 1.0 \times 10^{-3}$ g/cm^3, breakwater density $\rho_s = 0.5$ g/cm^3, meshsize 1500×280 for no breaking waves.

reflected wave height over the initial solitary wave height. The reflection and transmission coefficient can be easily calculated from Fig. 10 from peak value of gauges 1 and gauges 4, respectively.

The pressure distribution is useful to analysis the understanding of tsunami-induced damages and provide information for structural optimisation designs. Fig .10 (c) shows the pressure history on the pressure monitoring point A and B,

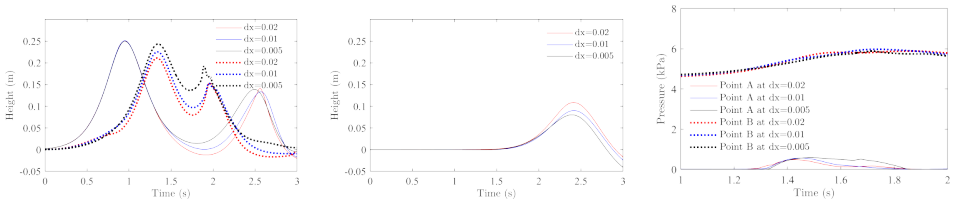

(a) (b) (c)

Figure 10: Convergence study of evolution of the free surface elevation at three locations (water gauges 1, 2 and 4.) for the solitary wave impact. Left: solid line: water gauges 1; dot line: water gauges 2. Middle: water gauges 4. Right: pressure history on point A and B.

as seen in Fig. 6. Fig. 11 shows time history of pressure distribution for solitary wave interaction with breakwaters. During the solitary wave impact on the breakwater, a clear discontinuous pressure distribution between the breakwater can be observed. There are no breaking waves and the pressure increases around 1 kPa for solitary wave height under $h = 0.25$ m.

steepness	breaking waves	transmission coef. (num.)	reflection coef. (num.)	Peak pressure (kPa)
0.1	no	0.59	0.33	0.0239 / 5.0034
0.2	no	0.54	0.38	0.0254 / 5.3561
0.3	no	0.50	0.43	0.0281 / 5.7563
0.4	no	0.45	0.47	0.0325 / 6.0197
0.5	yes	0.40	0.55	0.3843 / 6.2772
0.6	yes	0.35	0.66	1.3867 / 6.6672
0.7	yes	0.23	0.54	3.1196 / 6.9613

Table 5: Numerical result for transmission coefficient and reflection coefficient under different steepness. The simulations are performed under mesh resolution $dx = 0.01$ m.

Fig. 12 shows the time history of the pressure monitoring point A and B. In the non-breaking waves regime from $h = 0.1$ m to $h = 0.4$ m, the pressure loads at A are small. Table 5 summarise the transmission and reflection coefficients under 7 different wave heights. It is interesting to notice that with the increased wave steepness, the transmission coefficient decreases and the reflection coeffi-

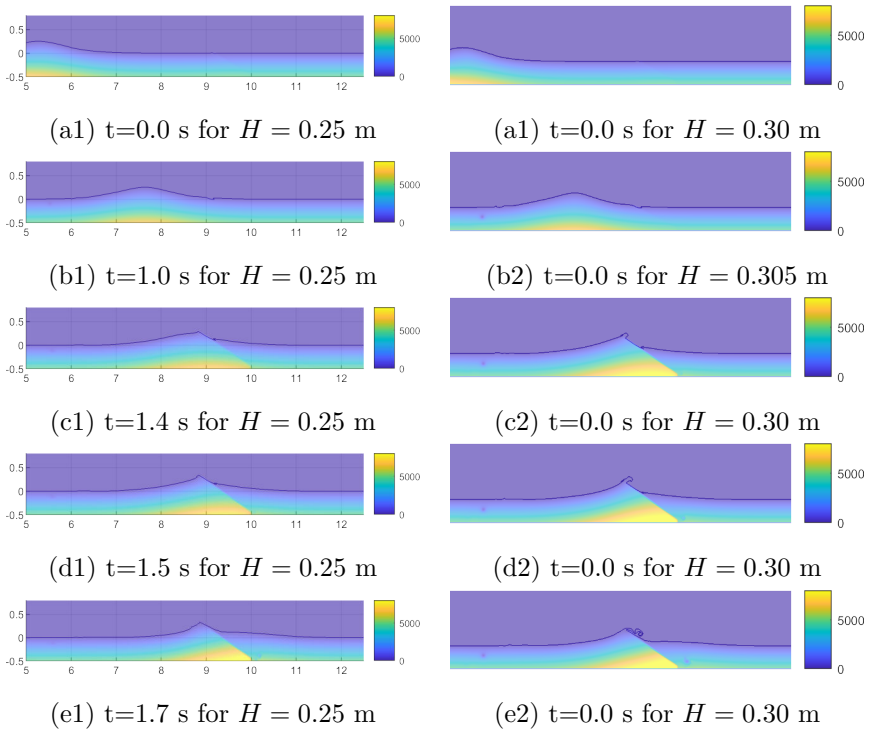

Figure 11: Time history of pressure distribution for solitary wave interaction with breakwaters at $h = 0.25$ m (left column) and $h = 0.3$ m (right column).

cient increases. The new type of breakwater shows a good property to prevent the extreme waves. Wave-overtopping and breaking waves can be observed for $h > 2.5$. Large slamming forces can be found for large wave height, which is more than 2 orders of magnitude compared with low wave height case.

6. Conclusions

The goal of this paper is to develop numerical simulation of wave transmission and reflection for a new flap-gate breakwater using the 'one-fluid' model. We have first reported the validation and convergence of numerical validation using airy, 2nd order Stokes and solitary wave theory. After that, the experiment allowed us to verify and validate for the wave-breakwater interaction under regular waves. A good agreement between computational results and experimental

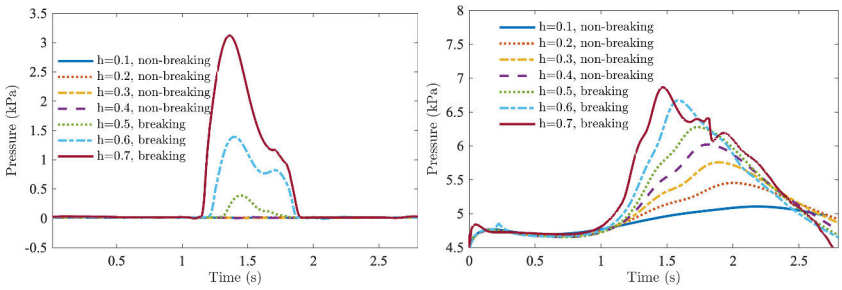

Figure 12: Time history of pressure monitoring point at point A (left) and point B (right) for different wave height from $h = 0.1$ m to $h = 0.7$ m.

data are shown. The numerical model can simulate free surface flow and wave breaking problems, the load/pressure producing processes. We also evaluate the performance of breakwater and impact pressure under different solitary waves for different wave heights. The numerical tool will be used for producing simplified relationships for tsunamis impact forces in codes of best practice.

Both experimental and numerical results illustrate that the 30 degree breakwater is the most efficient. There is no constraint on the flap's rotation motion, so the degree of breakwater is relied on the mass distribution. As a result, the efficiency of such systems may change with water depth, e.g. induced by the storm surge.

Author statements

S.G. CHEN: Conceptualisation, Software, Investigation, visualisation, Writing - Original Draft, project administration; L. Yang: Software, Formal analysis, writing—review and editing; J. Xing: Writing - Review & Editing; H. Zhang: Conceptualisation, Investigation, Supervision. Y.N. LUAN: Conceptualisation, Resources, Supervision; H.B. CHEN: Conceptualisation, Investigation, Supervision; H.Y. LIU: writing—original draft preparation, formal analysis.

Declaration of competing interest

The authors declare that they have no known competing financial interests or personal relationships that could have appeared to influence the work reported in this paper.

Acknowledgements

L. Yang acknowledges GCRF Fund 'Minimising the tsunami impact on coastal communities of developing countries' from Cranfield University. S.G. Chen acknowledges the National Natural Science Foundation of China (grant nos. 52001149, 52039005, 51861165102), National Key R&D Program of China (2018YFC0809604), Fundamental Research Funds for the Central Universities (KS20200203,TKS20210102, TKS2021011), the Young Elite Scientist Sponsorship Program by the China Association for Science and Technology (Grant No. 2018QNRC001).

References

[1] R. J. Nicholls, Planning for the impacts of sea level rise, Oceanography 24 (2) (2011) 144–157.

[2] Y. Qi, Y. Yang, F. Jin, China's economic development stage and its spatio-temporal evolution: A prefectural-level analysis, Journal of Geographical Sciences 23 (2) (2013) 297–314.

[3] N. L. Andrew, P. Bright, L. de la Rua, S. J. Teoh, M. Vickers, Coastal proximity of populations in 22 pacific island countries and territories, PloS one 14 (9) (2019) e0223249.

[4] G. Martinez, S. Costas, Ó. Ferreira, The role of culture for coastal disaster risk reduction measures: Empirical evidence from northern and southern europe, Advances in Climate Change Research (2020).

[5] T. Uda, Y. Hoshigami, S. Seino, H. Ozawa, Increase in disaster potential caused by excess use of land in coastal zone, Journal of Coastal Research (2007) 140–146.

[6] W. K. Laurent, N. Brown, B. Carvalho, F. Giles, B. Lodge, K. McBride, C. McGann, D. McLaughin, J. Peck, D. Tierney, et al., Development of a tool for assessing the vulnerability of rhode island's marinas to sea level rise and storm surge, in: Coastal Structures and Solutions to Coastal Disasters 2015: Resilient Coastal Communities, American Society of Civil Engineers Reston, VA, 2017, pp. 543–551.

[7] K. Udo, Y. Takeda, M. Takamura, A. Mano, Serious erosion of the southern sendai coast due to the 2011 tohoku earthquake tsunami and its recovery process, in: Post-Tsunami Hazard, Springer, 2015, pp. 225–236.

[8] W. R. Dally, J. Pope, Detached breakwaters for shore protection., Tech. rep., COASTAL ENGINEERING RESEARCH CENTER VICKSBURG MS (1986).

[9] D. K. Stauble, J. R. Tabar, The use of submerged narrow-crested breakwaters for shoreline erosion control, Journal of Coastal Research (2003) 684–722.

[10] M. A. Mustapa, O. Yaakob, Y. M. Ahmed, C.-K. Rheem, K. Koh, F. A. Adnan, Wave energy device and breakwater integration: A review, Renewable and Sustainable Energy Reviews 77 (2017) 43–58.

[11] J. Dai, C. M. Wang, T. Utsunomiya, W. Duan, Review of recent research and developments on floating breakwaters, Ocean Engineering 158 (2018) 132–151.

[12] T. Sawaragi, Coastal engineering-waves, beaches, wave-structure interactions, Elsevier, 1995.

[13] X. Zhao, D. Ning, Q. Zou, D. Qiao, S. Cai, Hybrid floating breakwater-wec system: A review, Ocean Engineering 186 (2019) 106126.

[14] I. N. Association, M. N. C. W. G. 28, Breakwaters with vertical and inclined concrete walls, no. 28, Pianc, 2003.

[15] K.-D. Suh, S. Shin, D. T. Cox, Hydrodynamic characteristics of pile-supported vertical wall breakwaters, Journal of waterway, port, coastal, and ocean engineering 132 (2) (2006) 83–96.

[16] G. Umgiesser, The impact of operating the mobile barriers in venice (mose) under climate change, Journal for Nature Conservation 54 (2020) 125783.

[17] G. Umgiesser, B. Matticchio, Simulating the mobile barrier (mose) operation in the venice lagoon, italy: global sea level rise and its implication for navigation, Ocean Dynamics 56 (3) (2006) 320–332.

[18] P. A. Pirazzoli, G. Umgiesser, The projected" mose" barriers against flooding in venice (italy) and the expected global sea-level rise, Journal of Marine Environmental Engineering 8 (3) (2006) 247–261.

[19] Y. Kimura, T. Wakunaga, M. Yasuda, H. Kimura, N. Kani, H. Mase, Development and verification of wall-flap-gate as tsunami inundation defence for nuclear plants, Nuclear Engineering and Design 323 (2017) 299–308.

[20] Y. Kimura, H. Mase, Numerical simulation of a rising seawall for coastal flood protection, Journal of waterway, port, coastal, and ocean engineering 140 (3) (2014) 04014002.

[21] Y. Kimura, K. Shimizu, M. Wani, M. Yasuda, H. Kimura, H. Mase, Development and installation of a flap-gate seawall against tsunamis, in: Coastal Structures and Solutions to Coastal Disasters 2015: Tsunamis, American Society of Civil Engineers Reston, VA, 2017, pp. 212–218.

[22] M. Darwiche, A. Williams, K.-H. Wang, Wave interaction with semiporous cylindrical breakwater, Journal of waterway, port, coastal, and ocean engineering 120 (4) (1994) 382–403.

[23] A. Williams, A. Abul-Azm, Dual pontoon floating breakwater, Ocean Engineering 24 (5) (1997) 465–478.

[24] X. Zhao, Y. Zhang, M. Li, L. Johanning, Hydrodynamic performance of a comb-type breakwater-wec system: An analytical study, Renewable Energy 159 (2020) 33–49.

[25] Y. Zhang, M. Li, X. Zhao, L. Chen, The effect of the coastal reflection on the performance of a floating breakwater-wec system, Applied Ocean Research 100 (2020) 102117.

[26] L. Yang, Prifysgol abertawe swansea university (2015).

[27] L. Yang, A. J. Gil, A. A. Carreño, J. Bonet, Unified one-fluid formulation for incompressible flexible solids and multiphase flows: Application to hydrodynamics using the immersed structural potential method (ISPM), International Journal for Numerical Methods in Fluids 86 (1) (2018) 78–106.

[28] C. Zhang, Z. Wu, C. Shen, Y. Zheng, L. Yang, Y. Liu, L. Ren, Effects of eigen and actual frequencies of soft elastic surfaces on droplet rebound from stationary flexible feather vanes, Soft Matter 16 (21) (2020) 5020–5031.

[29] L. Yang, A. Buchan, D. Pavlidis, A. Jones, P. Smith, M. Sakai, C. Pain, A three-phase interpenetrating continua approach for wave and porous structure interaction, Engineering Computations (2020).

[30] P. Higuera, J. L. Lara, I. J. Losada, Realistic wave generation and active wave absorption for navier–stokes models: Application to openfoam®, Coastal Engineering 71 (2013) 102–118.

[31] Z. Z. Hu, D. Greaves, A. Raby, Numerical wave tank study of extreme waves and wave-structure interaction using openfoam®, Ocean Engineering 126 (2016) 329–342.

[32] H. Bihs, A. Kamath, M. A. Chella, A. Aggarwal, Ø. A. Arntsen, A new level set numerical wave tank with improved density interpolation for complex wave hydrodynamics, Computers & Fluids 140 (2016) 191–208.

[33] G. Alfonsi, Reynolds-averaged navier–stokes equations for turbulence modeling (2009).

[34] L. Yang, One-fluid formulation for fluid–structure interaction with free surface, Computer Methods in Applied Mechanics and Engineering 332 (2018) 102–135.

[35] E. Renzi, K. Doherty, A. Henry, F. Dias, How does oyster work? the simple interpretation of oyster mathematics, European Journal of Mechanics-B/Fluids 47 (2014) 124–131.

[36] P. A. Madsen, D. R. Fuhrman, H. A. Schäffer, On the solitary wave paradigm for tsunamis, Journal of Geophysical Research: Oceans 113 (C12) (2008).

[37] W. Malfliet, Solitary wave solutions of nonlinear wave equations, American journal of physics 60 (7) (1992) 650–654.